Coupled Computational Fluid Dynamics and Multifilament Fiber-Spinning Model

Albert D. Harvey
Shell Exploration & Development, Houston, TX 77002

Antonios K. Doufas
Sunoco Inc., Pittsburgh, PA 15219

DOI 10.1002/aic.11066

A fundamental fiber-spinning model (proposed by Doufas and colleagues) is coupled to a three-dimensional Navier–Stokes computational fluid dynamics (CFD) code, where source terms for momentum and energy transfer between the fibers and the surrounding quench air are treated implicitly. The three-dimensional equations are solved for the airflow using a preconditioning technique in a structured multiblock framework. Scalable parallelism is achieved by assigning an arbitrary number of grid zones to a predetermined number of processors. Individual fibers are also divided equally among the available processors, allowing for thousands of fibers to be solved in only a few hours in realistic industrial-scale spinning processes. Model results are shown to agree with results obtained using Doufas et al.'s stand-alone fiber-spinning model in the limit of a small number of fibers. The coupled model is used to compute the temperature and air flow around individual fibers on a generic three-dimensional fiber-spinning application that contains multiple rows of fibers. It is found that, for large fiber bundles (such as 72 fibers) a significant variation in fiber cooling and tensile stresses exists across the bundle, which would result in significant variation in fiber tensile properties within the bundle. It is proposed that the cooling air velocity profiles across a multifilament system that exhibits stress-induced crystallization effects can be extracted from results obtained using the new coupled CFD/fiber-spinning model and can then be used in improved calculations (using a stand-alone fiber model) of the heat-transfer and air-drag coefficients within the fiber bundle. © 2006 American Institute of Chemical Engineers *AIChE J,* 53: 78–90, 2007

Keywords: multi-filament fiber spinning, polymer melt processing, computational fluid dynamics, convective cooling

Introduction

Fiber spinning is a polymer process of high industrial importance for converting a polymer melt into fibers. The molten polymer is drawn into thin fibers by a uniaxial drawing process, the capacity of which is a convolution of convective heat-transfer cooling processes, melt rheological response, and in many cases phase transformation (crystallization and molecular structure formation). Cooling fluid (typically air) is blown over the moving fibers as they are drawn from the polymer melt state. Typically, fiber speeds can be as high as 6 km/min (such as for polyamide systems) passing through a cooling chamber of 1–2 m in length. Heat-transfer rates must be sufficient so that the melt is effectively cooled to allow the drawn fibers to be wound on a spool or made into a nonwoven mat.

Correspondence concerning this article should be addressed to A. D. Harvey at albert.harvey@shell.com.

Convective heat-transfer and air-drag coefficients are critical to the simulation of fiber spinning to be successful in achieving quantitative agreement with spinline data, such as fiber velocity and temperature profiles. Traditionally, *empirical* heat-transfer relations are used[1,2] based on the correlation that was originally developed by Matsui.[3] The air-drag coefficient is then determined from the heat-transfer coefficient according to a momentum-heat analog.[2] These empirical heat-transfer correlations are primarily applicable to monofilament fiber-spinning processes. Anecdotal evidence suggests heat-transfer rates given by the Matsui correlation may be too high, although (probably for proprietary reasons) there has been little published discussion on this issue.[2]

Modeling efforts for multifilament melt spinning have been rather limited in the literature. In a multifilament system, complex interactions between the filament bundle and the quench air flow might occur, resulting in variations of the cooling profile from fiber to fiber in the bundle and subsequent variations in the spun-fiber properties. Dutta[4] developed a model for multifilament melt spinning of poly(ethylene terephthalate) fibers based on the approach of Yasuda et al.[5] In the multifilament model, empirical heat-transfer and air-drag coefficient correlations applied to the monofilament case were used, and the quench air velocity was reduced from fiber row to row as the air transversed the filament bundle, whereas the quench air temperature was assumed constant within the bundle.[4] The quench air velocity was adjusted for each filament row by applying local mass balances for the quench air phase. Along similar lines, Ishihara et al.[6] developed a model for a multifilament air jet melt-spinning process by estimating the profiles of quench air velocity and temperature from filament to filament in the bundle by the mass and energy balances in the air phase and applying those to the standard heat-transfer and air-drag correlations corresponding to the monofilament case.

The purpose of this article is to present a generalized simulation package for multifilament fiber spinning. This new model couples the quench airflow (air velocity and temperature) computed using computational fluid dynamics (CFD) for the flow around a multifilament bundle with the fundamental (that is, based on polymer kinetic theory) fiber-spinning model of Doufas et al.[7,8] The coupled model is rather general, being capable of handling an arbitrary number of fibers within the bundle (up to 1000 have been currently explored) and bundle geometry. CFD involves the representation of a flow domain into a discrete grid of computational cells, each having a finite size. The Navier–Stokes equations describing fluid motion are solved throughout this domain by considering mass, momentum, and energy conservation over each individual computational cell volume.

Herein we will make reference to modeling the drawing of molten polymer through dies and into single fibers as in Doufas et al.[7,8] and we refer to this type of model, which presumes a side-gas convective velocity and temperature, as a "stand-alone" model. We outline a procedure for directly computing the side-gas velocity and temperature of the cooling air, using a three-dimensional Navier–Stokes solver and couple the resulting cooling air velocity and temperature field with the solution to the individual fiber velocity, temperature, and stress profiles. We also outline a powerful distributed parallel technique of solving an arbitrary number of fibers. This three-dimensional Navier–Stokes solution of the cooling air coupled to the solution of the spinline velocity and temperature for an arbitrary number of fibers is referred to as a "coupled model."

Quench Air Flow Equations

Using standard notation for mean flow quantities and denoting pressure, Cartesian velocity components, specific internal energy, and total energy as p, u_β ($\beta = 1, 2, 3$), e, and $E_t = \rho[e + \frac{1}{2}\sum_\beta u_\beta^2]$, the conservative Reynolds-averaged Navier–Stokes equations for flow of a compressible fluid (quench air in our problem) can be concisely written in a generalized frame of reference, $\xi_\alpha = \xi_\alpha(x_\beta)$ ($\alpha, \beta = 1,2,3$) as

$$J\left(\frac{\partial \mathbf{Q}}{\partial t} + \Gamma\frac{\partial \mathbf{W}}{\partial \tau}\right) + \left(\frac{\partial \mathbf{H}_\alpha}{\partial \xi_\alpha}\right) = \mathbf{S} \tag{1a}$$

where the quantity $\mathbf{Q} = [\rho, \rho u_\beta, E_t]^\mathbf{T}$ represents the vector of conserved variables, $\mathbf{W} = [p, u_\beta, T]^\mathbf{T}$ is the vector of dependent variables (which includes the pressure, velocity components, and temperature of the cooling fluid), and J is the Jacobian of the curvilinear coordinate transformation defined below. The vector of source terms $\mathbf{S} = [0, F_{D\alpha}, q_f]^\mathbf{T}$ is attributed to the presence of the fibers in the cooling fluid flow field and is discussed further in the next section. It should be noted that a fully compressible formulation for the cooling airflow, although not necessary for the present applications involving the flow in fiber quench chambers, makes the code more applicable to problems involving general compressible and reacting gas flows involving density changes arising from chemical reaction and/or buoyancy effects. Low–Mach number preconditioning is used to provide a general means of solving the Navier–Stokes equations throughout the range of incompressible flow to fully supersonic compressible using a pseudocompressibility formulation to couple the pressure and velocity fields. The matrix Γ in Eq. 1a represents a suitable preconditioner, similar in form to that found in Shuen[9] and Edwards.[10] $\mathbf{H}_\alpha$ is the inviscid and viscous flux difference in the ξ_α coordinate direction:

$$\begin{aligned}\mathbf{H}_\alpha &= \mathbf{F}_\alpha^I + \mathbf{F}_\alpha^V \\ &= J\begin{bmatrix} \rho U_\alpha \\ \rho u_\beta U_\alpha + p\partial\xi_\alpha/\partial x_\beta \\ (E_t + p)U_\alpha \end{bmatrix} - J\begin{bmatrix} \partial\xi_\alpha/\partial x_\phi \\ \sigma_{\beta\phi}\partial\xi_\alpha/\partial x_\phi \\ (u_\beta\sigma_{\beta\phi} + q_\phi)\partial\xi_\alpha/\partial x_\phi \end{bmatrix}\end{aligned} \tag{1b}$$

The stress tensor is defined as $\sigma_{\alpha\beta} = -2\mu[S_{\alpha\beta} - \frac{1}{3}\,S_{\phi\phi}\delta_{\alpha\beta}]$ with $S_{\alpha\beta} = \frac{1}{2}\left(\frac{\partial u_\alpha}{\partial \xi_\phi}\,\frac{\partial \xi_\phi}{\partial x_\beta} + \frac{\partial u_\beta}{\partial \xi_\phi}\,\frac{\partial \xi_\phi}{\partial x_\alpha}\right)$. The quantity U_α is the contravariant velocity; $u_\beta(\partial\xi_\alpha/\partial x_\beta)$, the Fourier heat flux, is defined by $q_\phi = -\alpha_a(\partial T/\partial x_\phi)$; and J is the Jacobian of the curvilinear coordinate transformation, expressed as

$$J = \frac{\partial \xi_\alpha}{\partial x_\beta} = \begin{vmatrix} \xi_x & \xi_y & \xi_z \\ \eta_x & \eta_y & \eta_z \\ \zeta_x & \zeta_y & \zeta_z \end{vmatrix} \tag{1c}$$

The total effective viscosity includes molecular and turbulent components μ and μ_t, respectively. The molecular viscosity (μ) and thermal conductivity (α_a) of the cooling fluid can be described using arbitrary functions of temperature. For the present work the viscosity and thermal conductivity of the air are obtained using fourth-order temperature polynomials.[11] The turbulent eddy viscosity (μ_t) is obtained using a standard two-equation turbulence model, which will be briefly summarized below. The inviscid flux vector $\mathbf{F}_\alpha^I$ is separated into convective and pressure components using the second-order, low-diffusive, flux-spitting scheme (LDFSS) of Edwards.[10] A second-order backward three-point physical time differencing is used for the time-dependent term, a Euler differencing is used for the pseudotime derivative, and second-order central differences are used for the viscous terms. Equations 1a and 1b are linearized and the resulting system is solved using a zonal implicit ILU (individual location update) scheme. More details on the flow code are provided later.

The turbulent eddy viscosity μ_t is modeled using the standard two-layer k–ε model of Rodi and Mansour.[12] The transport equations for the turbulent kinetic energy k and turbulent dissipation rate ε can be cast in a form identical to Eqs. 1a and 1b, in which the conserved variable vector becomes $\mathbf{Q} = [\rho k,\ \rho\varepsilon]^{\mathbf{T}}$ and the dependent variable vector is $\mathbf{W} = [k,\ \varepsilon]^{\mathbf{T}}$:

$$\mathbf{H}_\alpha = \mathbf{F}_\alpha^I + \mathbf{F}_\alpha^V = J\begin{pmatrix} \rho k U_\alpha \\ \rho\varepsilon U_\alpha \end{pmatrix} - J\begin{bmatrix} (\mu + \mu_t/\sigma_k)\frac{\partial k}{\partial \xi_\phi}\ \frac{\partial \xi_\phi}{\partial x_\alpha} \\ (\mu + \mu_t/\sigma_\varepsilon)\frac{\partial \varepsilon}{\partial \xi_\phi}\ \frac{\partial \xi_\phi}{\partial x_\alpha} \end{bmatrix} \tag{2}$$

The source terms are given as

$$S = J\begin{bmatrix} \rho\tau_{\alpha\beta}\frac{\partial u_\alpha}{\partial \xi_\phi}\frac{\partial \xi_\phi}{\partial x_\beta} - \rho\varepsilon \\ C_1\rho(\varepsilon/k)\tau_{\alpha\beta}\frac{\partial u_\alpha}{\partial \xi_\phi}\frac{\partial \xi_\phi}{\partial x_\beta} - C_2\rho\varepsilon^2/k \end{bmatrix} \tag{3}$$

with $\tau_{\alpha\beta} = 2\mu_t S_{\alpha\beta}/\rho$. The turbulent eddy viscosity is defined in the standard fashion: $\mu_t = C_\mu \rho k^2/\varepsilon$. There are five constants in the model and the standard suggested values are used ($C_1 = 1.44$, $C_2 = 1.92$, $\sigma_k = 1$, $\sigma_\varepsilon = 1.3$, and $C_\mu = 0.09$). In the two-layer model, the eddy viscosity and turbulent dissipation rate are updated using a turbulent Reynolds number defined as $\mathrm{Re}_y = \rho\sqrt{k}\Delta y/\mu$, with Δy defined as the distance to the nearest wall. Additionally, turbulent length scales are defined as

$$l_\varepsilon = \frac{0.41\Delta y}{C_\mu^{3/4}}\left[1 - \exp\left(\frac{C_\mu^{3/4}\mathrm{Re}_y}{0.82}\right)\right] \tag{4a}$$

$$l_\mu = \frac{0.41\Delta y}{C_\mu^{3/4}}\left[1 - \exp\left(\frac{\mathrm{Re}_y}{70}\right)\right] \tag{4b}$$

In regions of the flow where $\mathrm{Re}_y > 200$ (near-wall regions), the dissipation rate is defined as $\varepsilon = k^{3/2}/l_\varepsilon$. The near-wall damping technique is also applied to the eddy viscosity in a similar manner. For $\mathrm{Re}_y > 200$, the eddy viscosity is set to $\mu_t = \rho C_\mu l_\mu \sqrt{k}$. For all other regions in the flow, the turbulent dissipation rate from the solution of its transport equation is used with $\mu_t = C_\mu \rho k^2/\varepsilon$.

Parallel Implementation

Three-dimensional computational analysis of industrial-scale fiber-spinning operations can be a significant challenge. Realistic computation of coupled fluid–fiber transport phenomena processes in commercial-scale equipment requires specialized computational tools. As computational resources become more powerful, computations with improved resolution and/or more chemical species (or fibers in our case) become more affordable. In chemical industry practice, the size of the problems can be very large such that, as speed and memory of computers increase, so does the size of the problem.

The present parallel code uses some advanced memory management strategies that allow fully implicit computation for large applications. The parallel implementation involves dividing the computational domain into a number of structured grid zones. Parallelization is accomplished by assigning one or more of these grid zones to a predetermined number of processors. In this manner memory can be reduced by simply cutting a zone in two pieces. On each processor, resident grid zones are computed in series. Matrix elements for each resident zone use the same memory for the implicit Jacobian calculations by overwriting the work done on previous zones. Thus, the total memory requirement of any single processor is proportional to the largest resident grid zone and not the whole portion of the domain. The drawback to this strategy is that Jacobian matrices must be recomputed at each iteration. For cases when the number of zones is equal to the number of processors, or when sufficient memory exists on each processor to store the entire Jacobian matrix for all resident zones, significant cost savings can be achieved. In rapidly changing regions of the flow and in the initial stages of a calculation, Jacobian matrices must be updated at every iteration for stability reasons. As calculations proceed toward convergence, it is possible to update computation of the Jacobian matrices every five to ten iterations, resulting in overall code speed-up by a factor of 3–4. Zonal interfaces (where two adjacent zones fit together) are updated by communication calls to the MPI code.

The present finite volume code solves the flow equations in a zonal manner. The solution domain is divided into an arbitrary number of hexagonal grid zones (Z). The parallel solution strategy partitions these domains among an arbitrary number of processors (P), with the requirement that $P \leq Z$. Each processor obtains a solution on its preassigned portion of the domain, subject to the boundary conditions for that part of the domain. Domain boundaries that are not physical boundaries obtain their data from the neighboring domains, either by in-memory data transfer when the domains reside on the same processor or through interprocessor data transfers when they reside on different processors. The interprocessor communication is accomplished by the industry-standard MPI protocol.[13]

Parallel efficiency is highly dependent on the application and can be controlled by the user in the grid generation step. Assignment of grid zones to a user-defined number of computers is automatic and is accomplished using METIS.[14] Applications that can be gridded using many zones of roughly the same size will exhibit a higher level of parallel efficiency. Data on the boundaries of each block are communicated to the boundaries of neighboring blocks at each iteration. The amount of information needed to update these interblock values is kept to a minimum. The parallel setup routines precompute the memory addresses of both the sources and destinations of all data transfer events, regardless of whether they reside in memory or exist on a different processor. Using these precomputed addresses, only the data values must be exchanged at each iteration, minimizing the communications overhead.

To minimize bottlenecks associated with latency time, all communication is performed using a single MPI communication call per iteration. Therefore message sizes are larger and communication parallel efficiencies are maximized, regardless of the protocol used (fast Ethernet, Gigabyte, or Myrinet). It was found that one large communication event per iteration is significantly more efficient than many smaller send/receive message pairs, especially so on the lower-cost protocols.

Processor memory requirements are halved when the size of the largest grid zone resident on a processor is halved and decrease as the number of resident zones on a processor decreases. The code requires no single master process that demands special memory considerations. The whole grid or solution is never resident on a single processor. Each processor needs memory proportional to only its largest resident grid zone. This ensures scalability and the only limitation is the number of available processors.

Parallel Implementation of Fiber Applications

Figure 1 illustrates a typical quench chamber geometry for fiber-spinning applications consisting of a rectangular-shaped domain. The domain is broken into a number of grid zones, each of which can be assigned to a different processor for the cooling gas flow-field solution. The left side illustrates an arbitrary multizone (block) computational grid containing seven fibers. In general, there may be an arbitrary number of grid zones that define the cooling air chamber and associated components of the fiber-spinning process. For computational efficiency these individual components of the computational domain may reside on different processors, thus facilitating an arbitrary level of grid density. Only the number of available processors limits the number of fibers capable of being considered in a single computation. The total number of fibers chosen is divided among the available processors as evenly as possible.

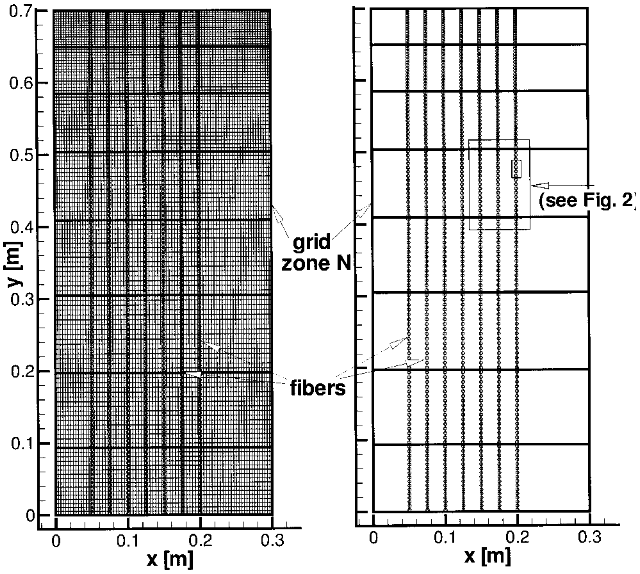

Figure 1. Multiblock computational mesh and fiber model construction (8 grid zones and 7 fibers).

The fibers are represented as a continuous linear string of particles. Exactly one particle per computational cell in the direction of the fiber length is provided. The fiber elements are modeled as discrete cylinders, each section of which contains a fiber particle at its center. The *N*th grid zone will contain a particular linear section of all the fibers for the purpose of obtaining the CFD solution for the cooling airflow field. However, for the solution of the fiber-spinning model,[7,8] which is embedded in the CFD code, the processor to which zone *N* is assigned will have only a preassigned number of whole fibers. The velocity and temperature fields for the quench air at different sections along these fibers are communicated to the processor in which the particular fiber is assigned. Thus efficient load balancing necessitates appropriate division of not only the computational grid zones, but also the individual fibers. The present technique uses the METIS algorithm[14] to allocate a balanced number of grid zones to the available number of processors. An algorithm is also used to partition grid zones that contain fiber sections as well as an algorithm to partition each individual fiber for solution of the one-dimensional fiber model. This multilevel parallel partitioning is scalable so that an arbitrary number of fibers and computational cells can be used.

There are two computational tasks involved: solution of the Navier–Stokes equations for the cooling gas flow field and solution of the conservation and constitutive equations for the fibers. The fiber equations (described next) are essentially one-dimensional (thin-filament approximation) formulated along each fiber line.

As an example of how the parallel coupling works, consider the left side of Figure 1. The quench chamber is divided into eight grid zones and each is (or can be) assigned to a different processor. We describe the solution procedure on grid zone *N* that may reside on processor *P*. In the solution of the gas-phase flow field, the equations are solved using a fully implicit block ILU scheme and boundaries of adjacent zones are communicated to neighboring processors using a ghost cell approach and MPI.[13] Source terms describing heat and momentum fluxes from the fiber elements contained in grid zone *N* are included in the calculations for all fibers. Each whole fiber is also assigned to a unique processor and the conservation/constitutive equations for the fiber are solved on this processor. To perform the calculations, each processor must first communicate the computed cooling air conditions (air temperature and air velocity) along the length of the resident section of each fiber to processor *P*.

A small section of the domain illustrated in the rectangle of Figure 1, is shown in more detail in Figure 2. Fibers are represented by a linear string of particles, each of which is the center of mass of a corresponding elemental fiber control volume. In general, the individual fiber particle elements are free to move in the *x*- and *z*-directions. This movement is constrained by the tension forces computed in the fiber-spinning model code for each fiber element. For the present work, we assume that the fibers remain stationary in the flow field at a fixed position in time. The right side of Figure 2 further illustrates the geometric details of the fiber and construction of the string of fiber elements. The finite-volume

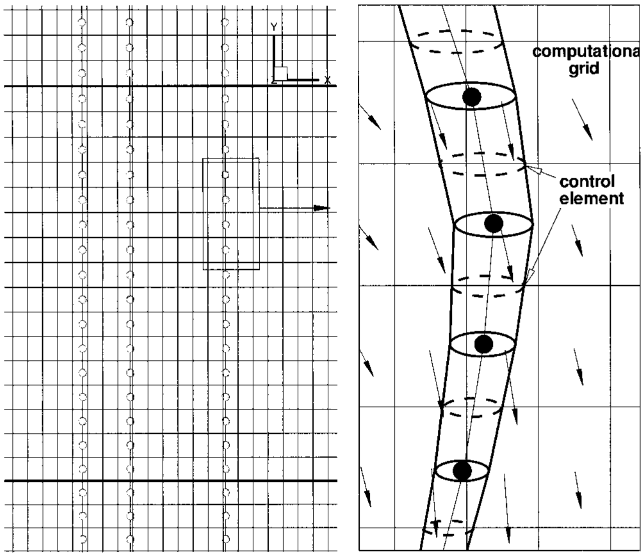

Figure 2. Fiber model construction details showing computational grid and fiber discretization.

CFD code provides local flow-field information at the cell centers of the computational mesh. A search algorithm is used to determine the location of each fiber particle. The velocity, temperature, and physical properties of the quench air are obtained at each fiber element location using an interpolation procedure. Heat and momentum transfer from the fiber element to the gas phase are then enforced at the grid cells in the vicinity of the fiber element location using a weighted distance function approach.[15]

Each fiber is discretized along its length through the domain as shown in Figure 2. Fiber particle elements are used to track the position of the fiber along its length. Computational grid zones through which the fibers pass are tagged for searching to determine the precise location of each fiber element during the course of the simulations.

Figure 3 illustrates a single fiber element of the fiber shown in Figure 2 and indicates the mass, momentum and energy balances of the process. In general, the fiber element is oriented arbitrarily and we define the local angle between the ith fiber element and the vertical y-axis as α_i. The fiber is parameterized along its length starting from the spinneret. The conservation of momentum for each element can be expressed as

$$\frac{d(\rho\forall_i)_f}{dt} = (\rho V A_c)_{f,i} - (\rho V A_c)_{f,i+1} \tag{5}$$

where ρ, V, A_c, and $\forall$ are, respectively, the density, velocity, cross-sectional area, and volume of the fiber element. The subscript f indicates quantities and physical properties of the fiber. As molten polymer cools and stretches, the cross-sectional area (diameter) of the produced filament is reduced, resulting in an increase in the fiber axial velocity. The volume of the ith fiber element can be expressed in terms of its diameter and orientation as

$$\forall_i = \frac{\pi L_i}{3\cos(\alpha_i)}(d_i^2 + d_i d_{i+1} + d_{i+1}^2) \tag{6}$$

A relationship for the cross-sectional area of the element as a function of the local fiber orientation and fiber diameter is

$$A_{c_i} = \frac{\pi d_i^2}{4\cos(\alpha_i)} \tag{7a}$$

$$A_{s_i} = \frac{\pi}{2}(d_i + d_{i+1})L_i \tag{7b}$$

The forces acting on a fiber element will include the total aerodynamic (drag) force $\vec{F}_A$ arising from the cooling airflow field, the gravitational force $\rho_f g\forall_i$ arising from the mass of the fiber element, and the rheological (viscoelastic) forces $\vec{F}_r$ in the fiber polymer.

$$\begin{aligned}\frac{\partial(\rho V\forall_i)_f}{\partial t} + [V(\rho V A_c)]_{f,i} \\ - [V(\rho V A_c]_{f,i+1} \\ = \vec{F}_{r_i} + \vec{F}_{r_{i+1}} + \vec{F}_A + \rho_f g\forall_i\end{aligned} \tag{8}$$

We note that this expression for the momentum balance has, in general, three separate components, one for each

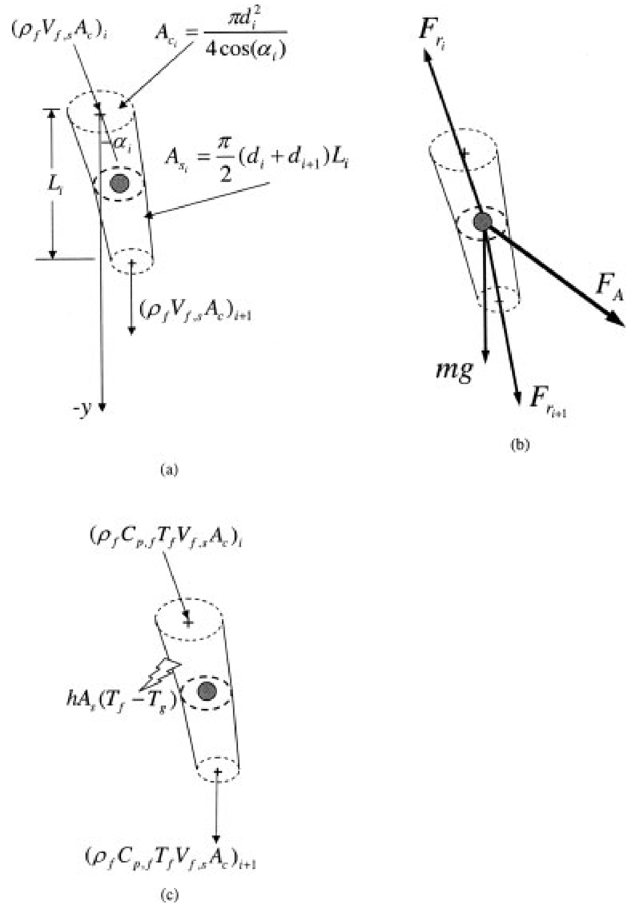

Figure 3. Fiber element showing (a) mass, (b) momentum, and (c) energy balances.

coordinate direction. For the aerodynamic force we consider tangential and normal components in the solution of the one-dimensional (cross-sectional averaged) fiber model above.

$$F_A^t = \frac{1}{2}\rho(V_f^t - V_g^t)V_f^t - V_g^t C_{D_t} A_s^t \tag{9a}$$

$$F_A^n = \frac{1}{2}\rho(V_f^n - V_g^n)V_f^n - V_g^n C_{f_n} A_s^n \tag{9b}$$

In these expressions, V_f and V_g are the velocity of the fiber and cooling air, respectively. Superscripts t and n indicate components tangential and normal to the fiber. The normal component of the cross-sectional area A_s^n of the element is that which is seen by the cross-flow component of the cooling air, whereas the tangential component is associated with the contribution to drag from the skin friction or viscous boundary layer around the fiber. These components of the cross-sectional area are written in terms of the diameter and fiber orientation angle α_i as follows:

$$A_s^t = \frac{\pi}{2}(d_i + d_{i+1})L_i \tag{10a}$$

$$A_s^n = \frac{1}{2}(d_i + d_{i+1})L_i \tag{10b}$$

Components of the air-drag coefficient are of the form $(C_D)_{n,t} = A\mathrm{Re}_{n,t}^B$, and can be found in the literature.[1,2,16] For now we disallow lateral motions of the fiber and motions along the length of the fiber in the s-direction are considered. Thus tangential components of the fiber velocity V_f^t will be neglected. For the purposes of coupling the effects of the presence of the fiber with the cooling gas phase, these forces must be resolved into Cartesian components. We also require derivatives of these Cartesian forces in our implicit gas-phase solution scheme. The rheological forces can be expressed in terms of the axial τ_{ss} and lateral stress τ_{rr} difference. The s-direction is defined axially along the fiber and the r-direction is normal to the fiber:

$$F_r = [A_c(\tau_{ss} - \tau_{rr})] \tag{11}$$

An expression for the conservation of energy inside the fiber element can be written as

$$\frac{\partial(\rho_f C_p T \forall_i)}{\partial t} + [V(\rho C_p T A_c)]_{f,i} - [V(\rho C_p T A_c)]_{f,i+1} = -hA_s(T_f - T_g) + (\tau_{ss} - \tau_{rr})\frac{\partial V_{f,s}}{\partial s} + \rho_f \Delta H_f V_{f,s}\frac{\partial \phi}{\partial s} \tag{12}$$

in which we consider the change in heat content from one end of an element to the other as the combined sum of the convection heat transfer from the cooling air surroundings, the work done on the polymer in stretching and deformation (viscous dissipation) and the heat arising from phase change of the polymer (crystallization effects). The quantity ϕ is the degree of crystallinity in the polymeric material. In the energy balance equation, C_p is the specific heat of the fiber material, h is the convective heat-transfer coefficient, and ΔH_f is the change in enthalpy arising from the phase change. Because crystallization effects are insignificant in the present analysis, the last term on the right-hand side of Eq. 12 is set to zero. More discussion on the mechanisms of heating can be found in Doufas et al.[7,8]

The coupled CFD/fiber-spinning model algorithm can be summarized as follows:

(1) Initialize the position, velocity, diameter, and temperature of each fiber and compute source terms for the momentum and energy equations (this step should be performed only once). Boundary conditions of the fiber-spinning model are described in Doufas et al.[7,8]

(2) Perform iteration on the flow field using the CFD code using source terms computed in the previous step.

(3) Perform search for each particle location.

(4) Interpolate values of velocity and temperature to each fiber particle location.

(5) Compute heat-transfer and air-drag coefficients at each fiber particle location.

(6) Gather all fiber segments from slave processes and send drag and heat-transfer coefficients to the master process containing each fiber.

(7) Using the fiber-spinning model,[7,8] perform an iteration on each fiber computing an updated fiber temperature, fiber velocity, fiber viscoelastic stress, and diameter at each fiber element.

(8) Communicate the new fiber velocity and fiber temperature to the slave processors for each fiber section.

(9) Construct source terms attributed to momentum and energy exchange from each fiber element to the gas phase (Eq. 1a) and index the appropriate computational cell, adding appropriate contributions to the left-hand side of the equations; then return to step 2.

Material Input Parameters and Correlations

The resin studied in this work is a generic polyethylene melt of a 3.5 g/10 min melt index (ASTM D1238, 190°C/2.16 kg), considered to be a relatively slow crystallizing material with a differential scanning calorimetry (DSC) peak crystallization temperature of nearly 50°C (thermal scan of 10°C/min) and an absolute crystallinity of <10%. In addition, because of the slow speed spinning conditions considered in this work (take-up speed of 325 m/min), stress-induced crystallization (SIC) is expected to play a minor role in the studied cases. Therefore, crystallization effects are neglected in the modeling and the amorphous portion of the Doufas et al.[7,8] two-phase constitutive formulation is considered, that is, the melt is modeled with a *modified* Giesekus constitutive equation.

The zero-shear-rate viscosity η_0 of the melt is calculated according to the Arrhenius relationship and the time-temperature superposition principle as follows[17]:

$$\eta_0(T) = \eta_0(T_{ref})\exp\left[\frac{E_{act}}{R}\left(\frac{1}{T} - \frac{1}{T_{ref}}\right)\right] \tag{13}$$

where R is the ideal gas constant. The rheological parameters used for model simulations are summarized in Table 1.

As previously discussed in the literature,[18] in extensional flows an average should be weighted toward higher relaxation times (more than in shear flow kinematics). Moreover, for the simpler theories leading to critical values of Weissenburg numbers for multiple relaxation times (that is, Maxwell

Table 1. Rheological Parameters of Generic Polyethylene Melt Used in Model Simulations*

Parameter	Value
Zero-shear-rate viscosity, η_0 (Pa·s)	2800
Reference temperature, T_{ref} (°C)	190
Activation energy for flow, E_{act} (kJ/mol)	40
Characteristic modulus, G (Pa)	900
Molecular mobility parameter, α	0.23
Chain finite extensibility parameter, N_0	25

*From Doufas.[16]

type of models), the longest relaxation time is reported as the most relevant to extensional deformation.[18] Therefore, we consider that the studied polyethylene melt can be described by one characteristic conformation tensor **c** (the second moment of the chain end-to-end distance),[7,8,16] corresponding to a relaxation timescale characteristic of the elongational flow (closer to the longest relaxation time) and therefore a characteristic modulus of elasticity G (see Table 1). For more details, the reader is referred to Doufas.[16]

The heat capacity of the melt is expressed as a linear function of T (°C) as follows:

$$C_p(T) = C_{l1} + C_{l2}T \tag{14}$$

where $C_{l1} = 0.506$ cal/(g °C), $C_{l2} = 0.00068$ cal/(g °C^2) for polyethylene melts.[19] The surface tension was taken as 0.0265 N/m.[19]

The convective heat-transfer coefficient h for the stand-alone model (that is, model without CFD using semiempirical transport correlations) is calculated from the following correlation for the Nusselt (Nu) number applied to monofilament fiber spinning[2]:

$$\mathrm{Nu} = \frac{hD}{\alpha_a} = 0.3\,\mathrm{Pr}^{1/3}\left(\frac{\rho_a v_z D}{\eta_a}\right)^{0.39}\left[1 + \left(\frac{8u_{a,x}}{v_z}\right)^2\right]^{1/6} \tag{15}$$

where α_a, ρ_a, and η_a represent, respectively, the thermal conductivity, density, and viscosity of the air at an arbitrary position z; $u_{a,x}$ is the component of the air velocity perpendicular to the fiber (cross-component). The Prandtl number (Pr) for air over the entire range of likely interest (20–290°C) varies only between 0.68 and 0.71, so $\mathrm{Pr}^{1/3}$ is essentially constant at 0.885.[2] The heat-transfer coefficient correlation proposed by Denn[2] is more realistic than the original one developed by Kase and Matsuo,[20] which appears to overpredict the convective heat-transfer coefficient.[2] The air-drag coefficient C_f for the stand-alone program is calculated as follows[2]:

$$C_f = 0.6\left(\frac{\rho_a v_z D}{\eta_a}\right)^{-0.61} \tag{16}$$

The processing conditions used in the simulations for the coupled CFD/fiber-spinning model are summarized in Table 2.

Table 2. Processing Conditions for Coupled CFD/Fiber-Spinning and Stand-alone Model Simulations

Condition	Value
Die diameter, D_0 (mm)	0.8
Take-up speed, v_L (m/min)	325
Mass throughput, W (g^{-1} min^{-1} hole^{-1})	1.44
Die temperature, T_0 (°C)	290
Quench delay (mm)	7.5
Active quench chamber length (m)	1.48
Spinline length, L (m)	4
Quench air temperature, T_a (°C) from quench screen	20
Cross quench air velocity (m/s from quench screen)	0, 0.5
Down tangential quench air velocity (m/s from quench screen)	0
Number of simulated fibers	1, 6, 24, 72

Results and Discussion

As a consequence of the lack of fiber-spinning data in a multifilament configuration, no direct comparison with data is made in this work, as is also the case with other works.[4] Our objective is to demonstrate the physics captured by the coupled CFD/fiber-spinning model relative to the stand-alone model, where imposed air velocity and air temperature profiles across the fiber corresponding to inlet air flow conditions are considered.

In this section we test the coupled CFD/fiber model with the results using the stand-alone fiber model. The geometry, shown in Figure 4, consists of a rectangular cooling chamber

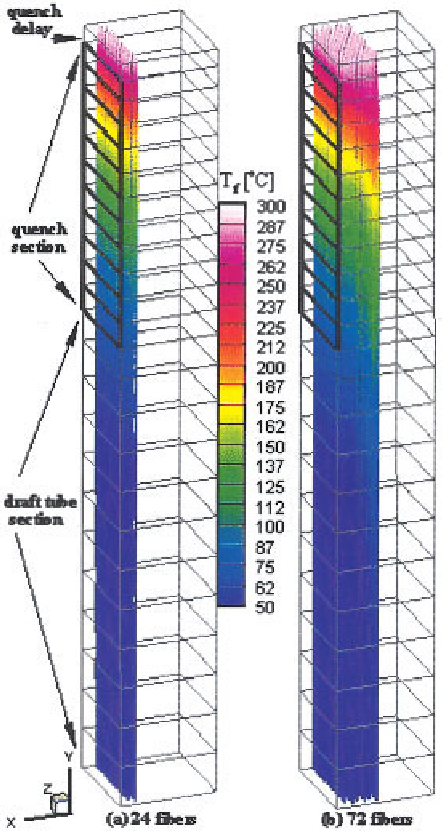

Figure 4. Three-dimensional cooling chamber with: (a) 24 grid zones and 24 fibers; (b) 24 zones and 72 fibers.

[Color figure can be viewed in the online issue, which is available at www.interscience.wiley.com.]

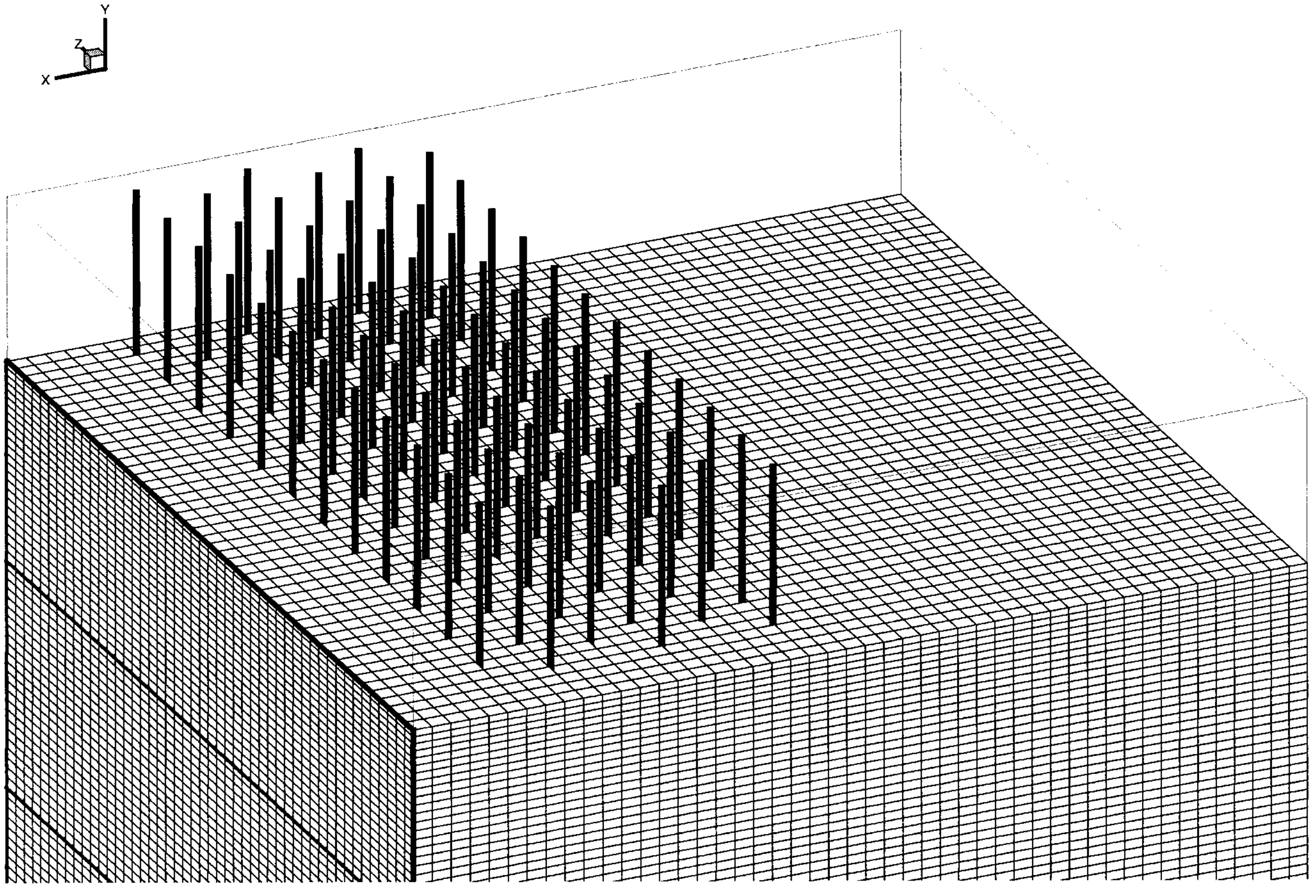

Figure 5. Close-up of top of the cooling chamber showing six staggered rows of 12 fibers.

containing 24 zones and 24 fibers (Figure 4a) and a case involving 72 fibers (Figure 4b). The fibers were arranged in two staggered rows each containing 12 fibers (Figure 4a) and six staggered rows of 12 (Figure 4b). Calculations were performed on 24 Linux processors; each processor was assigned one computational zone and one fiber (or three fibers for the 72-fiber case). As in the two-dimensional example case, all physical boundaries were treated as no-slip walls except one side face of zones 2–12 (heavy black boundaries) that were designated as inflow and the bottom face of zone 24 (lowermost zone) was treated as outflow. The region above the inlet section (upper zone in Figure 4) is commonly referred to as the *quench delay* section. For this zone no-slip boundaries were imposed on all faces except the bottom face is an interblock boundary. Zones 2–12 make up the quench zones (inflow through one face) and the 12 lower zones make up the draft tube (no-slip on all faces except top and bottom). Flow enters from the right side through the quench sections shown by the heavy solid grid zone faces. Fibers are colored by the local value of the computed temperature. Note that back rows in Figure 4b are significantly warmer farther down in the cooling chamber. We will show this in more detail later. The model quench chamber, constructed for the purpose of illustrating the present computational techniques, was 48 cm in cross section and 390 cm in length. Spacing between fiber rows in the streamwise or x-direction was assumed to be 3 and 3.7 cm in the cross-flow and z-direction, respectively.

Figure 5 illustrates a close-up of the upper portion of the cooling chamber with 72 fibers. The (uppermost) grid for the zone representing the quench section (top-most grid zone) is not shown to clearly illustrate the positioning and spacing of the actual fibers (that pass through this zone) in relation to the computational grid. As discussed in the previous section, one fiber element per computational cell in the vertical direction is used to represent each fiber. Each of the 24 computational zones contains 48 computational cells in each lateral direction and 24 computational cells in the vertical direction (along the fibers). Larger grids were also used and the sensitivity of the coupled CFD model to different grid sizes was studied and the results will be presented later. Figure 5 depicts the relative length scales of the problem. Typical fiber diameters are on the order of tens to hundreds of microns (and thus are not shown to scale in any of the figures) and full resolution of the fibers using the computational grid would be impractical (or practically impossible). As stated earlier, the effects of the presence of the fibers on the gas-phase flow field is captured using source terms in the momentum equations, which are proportional to expressions for the frictional and drag forces on the fibers.

To test the implementation of the fiber-spinning model in the CFD code, we compare results obtained using the

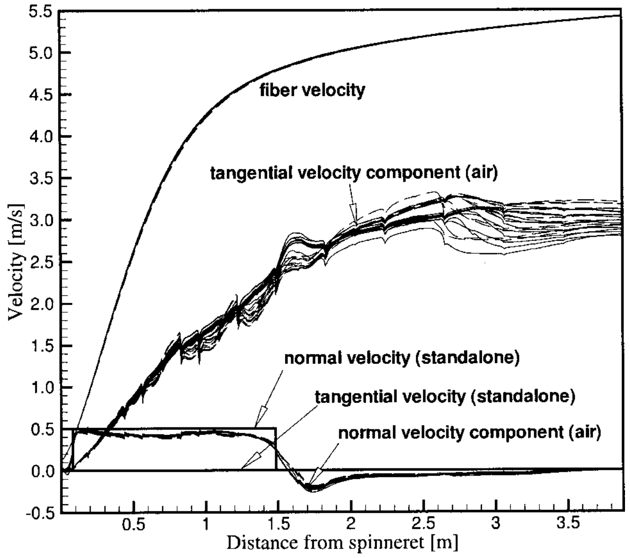

Figure 6. Fiber velocity and quench air velocity at the fiber location.

coupled CFD/fiber model with results obtained using the stand-alone fiber model[7,8] for the cooling chamber geometry shown in Figure 4. In the stand-alone model, the quench chamber air flow was assumed to be uniform and normal to the fibers in the quench zone region only (see Figures 4 and 5). Both in the quench delay and in the draft tube sections, the normal velocity was assumed to be zero for the stand-alone model. Calculations were performed with the magnitude of the cross-flow air in the quench zone set at both 0.0 and 0.5 m/s.

Figure 6 shows the fiber and gas velocity at the fiber locations for all 24 fibers and the geometry introduced in Figures 4 and 5. Fiber temperature and the temperature of the air at the location of each fiber are illustrated by separate curves in Figure 6. Note that the computed fiber velocity using the coupled models is almost identical for all 24 fibers. Lines in the figure illustrate the normal and tangential (to the fiber) air velocity imposed by the simplified stand-alone model, in which the tangential velocity is identically zero. The actual tangential velocity components computed by the coupled CFD model are quite different from those assumed in a typical stand-alone simulation. Note that the normal velocity is negative just below the bottom of the quench section as a result of the separation region that exists. The tangential component of the gas velocity at the fiber location is high because of the effect of the moving fibers. The coupled CFD model takes into account the acceleration of the cooling air by the fiber movement. Thus the relative velocity between the cooling air and the fiber is less than that predicted with conventional stand-alone fiber modeling, which does not consider the effects of the fiber velocity on the cooling airflow.

Figure 7 shows results for the fiber temperature as a function of distance from the spinneret for both cases with 0.0 and 0.5 m/s cross-flow air for a single filament simulation. The stand-alone fiber model results are shown using symbols and the coupled CFD results are shown using curves. Note that the agreement is good, as it should be, considering that the same fiber constitutive model is used for each calculation. Grid consistency is illustrated by the solid and the dash–dot–dot curves that compare fiber temperature results at different computational grid densities. The dash–dot–dot curve represents results using a 64 × 64 × 24 computational grid (in each of the 24 grid zones = 2,359,296 cells), whereas the solid curve represents results obtained using a 48 × 48 × 24 computational grid (1,327,104 cells). Total resolution along the vertical direction for both grids was 24 × 24 = 576 vertical grid layers. Because all results were essentially equivalent for both grids, the smaller grid was used in all subsequent simulations.

The dash–dot curve in Figure 7 shows temperature results using the coupled CFD model but with the inlet flow set to (machine) zero. These results also agree well with the stand-

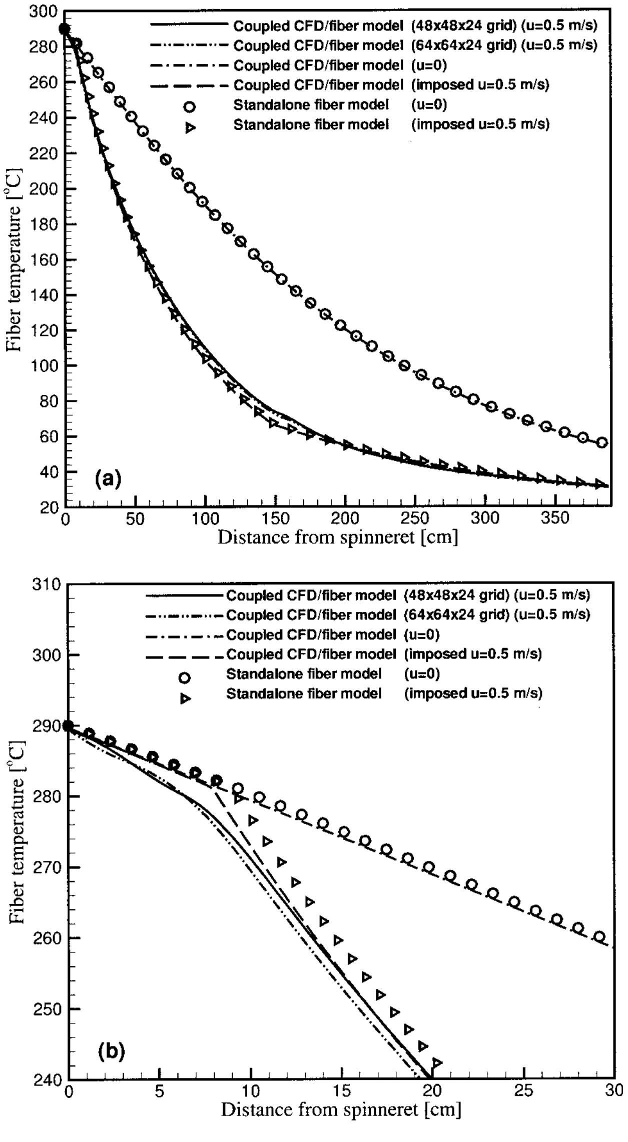

Figure 7. Comparison of coupled and stand-alone results for single fiber.

(a) Fiber temperature; (b) fiber temperature in quench delay section (top of quench chamber).

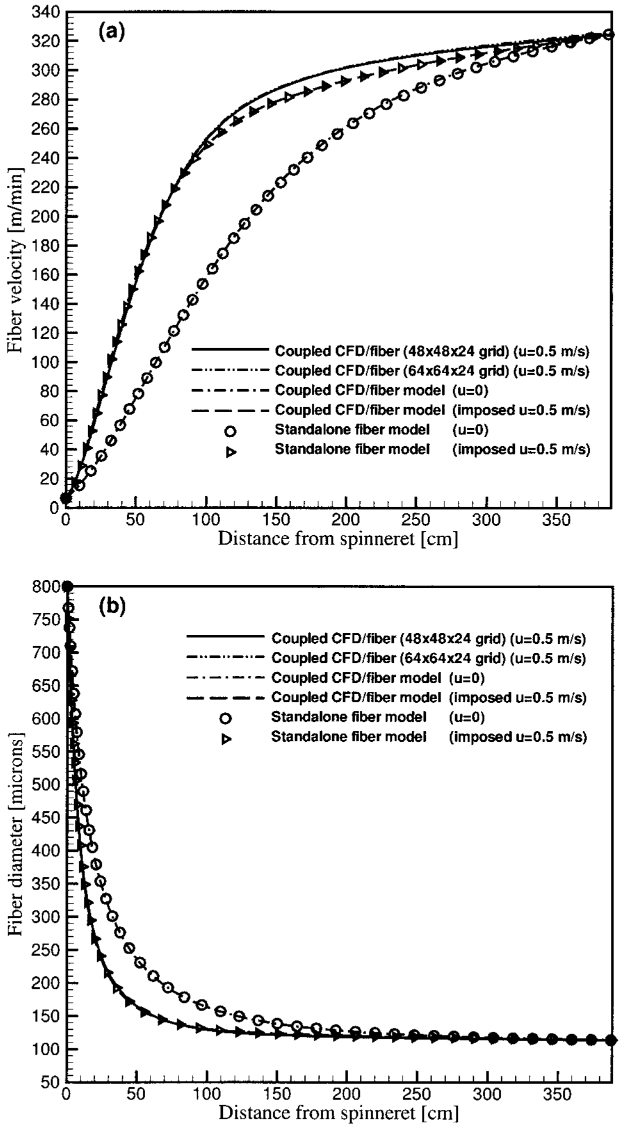

Figure 8. Comparison of coupled CFD/fiber model (this work) and stand-alone results of Doufas et al.[7,8] for single fiber.

(a) Fiber velocity; (b) fiber diameter.

alone model calculation with an imposed zero flow (circles). The dashed curve shows coupled CFD results using an imposed 0.5 m/s normal airflow in the quench zone and zero flow in the quench delay and spinline sections below the quench chamber (that is, the flow field was frozen at the conditions imposed in the stand-alone model). Once again, results agree well with the stand-alone model results obtained with 0.5 m/s imposed flow (triangles). The temperature of the fiber is cooler when the imposed flow is higher, as expected. Figure 7a shows the entire fiber line, whereas the Figure 7b shows the results in the top portion of the quench chamber near the quench delay section. Note for the triangle symbols (stand-alone model with 0.5 m/s imposed normal velocity in the quench section only), there is a slope change in the temperature profile at the two locations along the fiber model where the velocity is discontinuous (see solid curve of Figure 7). This feature also exists in the dashed curve, which is the result of the coupled model with the same imposed flow field. This feature is absent in the zero flow case (circle symbols and zero airflow dashed curve). Note in the coupled CFD/fiber simulation results, the slope change at these locations is less abrupt and more physical because the velocity is computed using the CFD code and is no longer discontinuous as in the stand-alone program. Besides these features, the results are essentially the same, confirming the accuracy in the implementation of the fiber-spinning model into the CFD code.

Figure 8 illustrates comparisons between the stand-alone and coupled CFD models for the fiber velocity (Figure 8a) and fiber diameter (Figure 8b). Note that the stand-alone model agrees well with the stand-alone fiber model for fiber velocity and diameter for both idealized flow-field conditions (zero flow and 0.5 m/s in the quench zone only). The solid and dash–dot–dot curves show the fiber velocity and diameter with the fully coupled flow field. The dash–dot–dot curve represents results using a 64 × 64 × 24 computational grid (in each of the 24 grid zones), whereas the solid curve represents results obtained using a 48 × 48 × 24 computational grid. The fiber velocity increases faster and the fiber diameter decreases faster when the fiber is cooled more rapidly.

Figure 9 shows fiber temperatures for each of 72 fibers (six staggered rows of 12 fibers) as a function of the distance from the spinneret for the configuration illustrated in Figures 4 and 5. Figure 9a shows fiber temperatures for the entire spinline, whereas Figure 9b illustrates a close-up of the fibers nearest the spinneret. The fibers are illustrated by their relative position in the quench chamber. Small temperature variations are observed for fibers in a common row. The stand-alone model results obtained using the idealized flow-field conditions are shown by the curve with symbols. Note that the temperature distributions for the upstream-most two rows compare well with Figure 7. Significant temperature differences exist between the 12 fibers in the front row and the 12 fibers that are members of the back (downstream) row. The small kink in the temperature profiles along the fibers is located at the boundary between the quench region and the draft tube (cross-stream flow ends and the draft tube section starts). Note that the draft tube refers to the section of the spinline between the take-up rolls and the bottom of the quench chamber. There is a small flow separation and recirculation zone at this location. The stand-alone model predicts the strongest fiber cooling effect, which is intrinsic to the assumed (idealized) inlet airflow profile, neglecting tangential airflow components (captured by the CFD/fiber model).

Figure 10 illustrates the velocity magnitude computed using the coupled CFD/fiber model. Figure 10a shows the case containing 24 fibers (two rows of 12) and Figure 10b shows the case that contains 72 fibers (six rows of 12). Note that in each case, cooling air enters the chamber from the left at 0.5 m/s as indicated. The downward air velocity is highest in the lower part of the chamber and in the vicinity of the fibers. Note the small recirculation region below the entrance for each case. For the case with 72 fibers the air velocity is lower on the right side of the chamber because of the larger downward draft of the larger fiber bundle. The

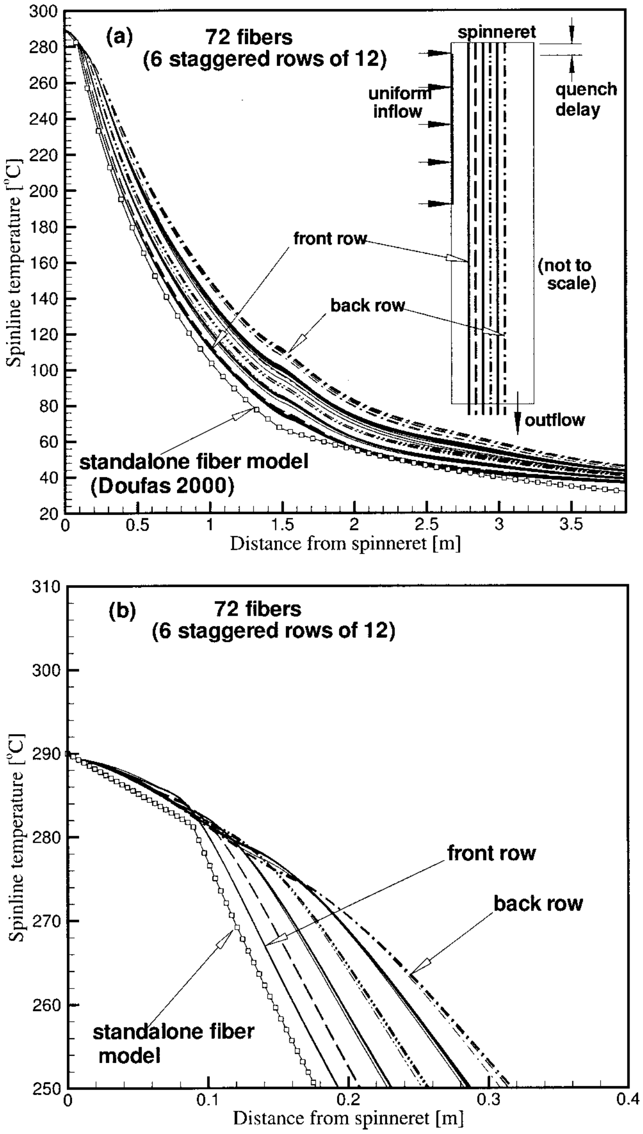

Figure 9. Fiber temperature computations for 72 fibers (six rows of 12 each).

larger combined total mass of the 72 fiber system results in an induced downdraft that tends to produce an adverse pressure gradient in the lower right portion of the draft tube, suggesting the cooling air flow is insufficient. The velocity penetrates farther into the chamber for the smaller fiber bundle. Figure 10 also shows that in the 72-fiber system, the air flow is more disturbed and deviates from the inflow cross-flow relative to the 24-fiber case.

Figure 11 shows the cooling gas temperature fields. The temperature is significantly higher in the upper portion of the chamber and in the back of the chamber for the case containing 72 fibers. This case illustrates the need for a higher mass flow of cooling air when the fiber bundle becomes larger to sufficiently cool all fibers of the bundle.

In Figure 12, the predicted profiles of tensile stress at various locations with the 72-fiber bundle are depicted. It is shown that the fibers that are closer to the quench air entrance (denoted as "outer fibers") exhibit higher tensile stress than that of the fibers at the center of the bundle (denoted as "inner fibers"). The fibers between the "outer" and "inner" fibers of bundle denoted as "middle fibers" demonstrate an intermediate tensile stress profile, as expected. The tensile stress profiles are consistent with the fiber temperature profiles of Figure 9. The "outer" fibers experience the highest degree of cooling, resulting in the highest polymer relaxation times and thus the highest molecular orientation and tensile stress. A difference of roughly 45% in frozen orientational stress is expected to result in significant variation of fiber tensile properties (such as elongation to break and tenacity) within the bundle. This is an interesting feature of the coupled CFD/fiber model vs. the stand-alone program where the quench airflow profile is assumed to be uniform within the fiber bundle, thus resulting in prediction of a uniform tensile stress profile and thus properties for all fibers.

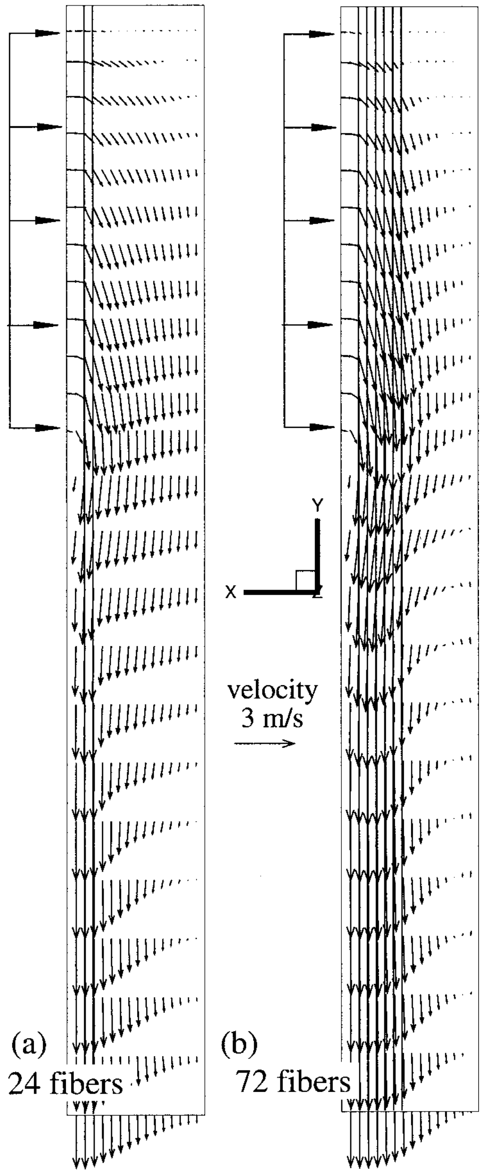

Figure 10. Quench air velocity field for 24 fibers.

(a) Two staggered rows of 12; (b) 72 fibers, six rows of 12.

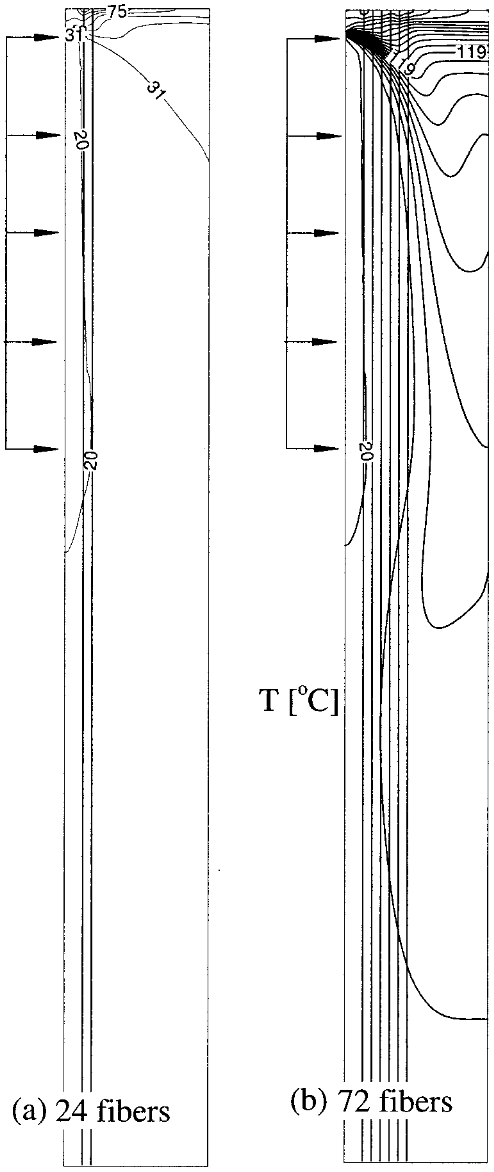

(a) 24 fibers

(b) 72 fibers

Figure 11. Cooling air temperature field.

(a) Twenty-four fibers, two staggered rows of 12; (b) 72 fibers, six rows of 12.

Conclusions

A fundamental fiber-spinning model[7,8,16] is coupled to a three-dimensional Navier–Stokes computational fluid dynamics (CFD) code, where source terms for momentum and energy exchange between the fibers and the surrounding quench air are treated implicitly. The three-dimensional equations are solved for the airflow using a preconditioning technique in a structured multiblock framework. Scalable parallelism is achieved using the METIS decomposition algorithm to assign an arbitrary number of grid zones to a predetermined number of processors. Individual fibers are also divided equally among the available processors, allowing for thousands of fibers to be solved in only a few hours in realistic industrial-scale spinning processes. Model results are shown to agree with results obtained using the stand-alone fiber model in the limit of small number of fibers (say, <24). The coupled model is used to compute the temperature and air flow around individual fibers on a generic three-dimensional fiber-spinning application that contains multiple rows of fibers. It is found that, for large fiber bundles (say, 72 fibers) significant variations in fiber cooling and tensile stresses exist across the bundle. This is expected to result in significant variation in fiber tensile properties such as elongation to break and tenacity within the bundle.

It is proposed that the coupled CFD/fiber model presented here potentially be used to extract the air velocity profiles across a multifilament bundle of an amorphous material that does not exhibit crystallization effects. To a first approximation, considering that the air velocity profiles of the amorphous system should be similar for a system of similar geometry (in terms of quench chamber and fiber bundle configuration) that exhibits stress-induced crystallization physics, we can use such air velocity profiles to locally calculate the heat-transfer and air-drag coefficients for each fiber of the multifilament system, thus applying a pseudomonofilament approach for the multifilament system. The other crystallization related parameters of the Doufas et al.[7,8] model (such as F and ξ) could be applied in the multifilament case for all the fibers in the bundle because they are material characteristics and therefore should be independent of fiber location in the bundle or bundle configuration. This approach is envisioned to result in enhanced predictive capability of complex multifilament fiber-spinning models without the need to adjust the material parameters, rather focusing on refining the assumption with respect to the quench air velocity profiles and heat-transfer coefficients within the bundle. Demonstration of this concept might be the topic of a future investigation.

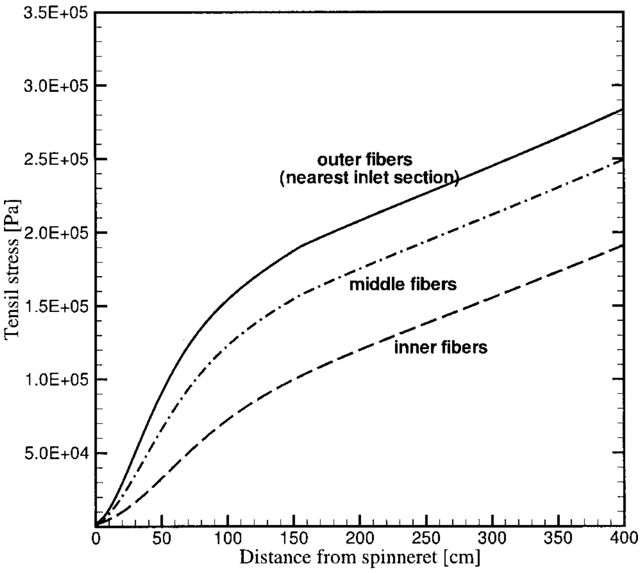

Figure 12. Fiber tensile stress profile computations for various positions within 72 fiber bundle (six rows of 12 each) from the coupled CFD/fiber model.

Literature Cited

1. Denn MM. Fibre spinning. In: Pearson JRA, Richardson SM, eds. Computational Analysis of Polymer Processing. London: Applied Science Publishers; 1983:179–216.
2. Denn MM. Correlations for transport coefficients in textile fiber spinning. *Ind Eng Chem Res*. 1996;35:2842–2843.
3. Matsui M. Air drag on a continuous filament in melt spinning. *Trans Soc Rheol*. 1976;20:465–473.
4. Dutta A. Role of air profiles in multifilament melt spinning of PET fibers. *Textile Res J*. 1987;57:13–19.
5. Yasuda H, Ishihara H, Yanagawa H. Computer simulations of melt spinning and its application to the actual process. *Sen-I-Gakkaishi*. 1978;34:20–27.
6. Ishihara H, Hayashi S, Ikeuchi H. Computer simulation of multi filament air jet melt spinning. *Int Polym Process*. 1989;2: 91–95.
7. Doufas AK, McHugh AJ, Miller C. Simulation of melt spinning including flow-induced crystallization. Part I. Model development and predictions. *J Non-Newtonian Fluid Mech*. 2000;92:27–66.
8. Doufas AK, McHugh AJ, Miller C, Immaneni A. Simulation of melt spinning including flow-induced crystallization. Part II. Quantitative comparisons with industrial spinline data. *J Non-Newtonian Fluid Mech*. 2000;92:81–103.
9. Shuen J-S, Chen K-H, Choi Y. A coupled implicit method for chemical non-equilibrium flows at all speeds. *J Comp Phys*. 1993;106: 306–318.
10. Edwards JR. A low-diffusion flux-splitting scheme for Navier–Stokes calculations. *Comput Fluids*. 1997;26:645–659.
11. McBride BJ, Gordon S, Reno MA. Coefficients for calculating thermodynamics and transport properties of individual species. National Aeronautics and Space Administration (NASA) Technical Memorandum 4513. Washington, DC: NASA; 1993.
12. Rodi W, Mansour NN. Low Reynolds number k–ε modelling with the aid of direct simulation data. *J Fluid Mech*. 1993;250:509–529.
13. Gropp W, Lusk E, Skjellum A. Using MPI, Portable Parallel Programming with Message Passing Interface. 2nd Edition. Cambridge, MA: The MIT Press; 1999.
14. Karypis G, Kumar V. METIS: A software package for partitioning unstructured graphs, partitioning meshes, and computing fill-reducing orderings of sparse matrices. Minneapolis, MN: University of Minnesota; 1998.
15. Tyagi M, Roy S, Harvey AD, Acharya S. Simulation of turbulent impeller stirred tanks using immersed boundary method and large eddy simulation technique in multi-block curvilinear geometries. *Chem Eng Sci*. 2006;61:000–000.
16. Doufas AK. Analysis of the rheotens experiment with viscoelastic constitutive equations for probing extensional rheology of polymer melts. *J Rheol*. 2006;50:749–769.
17. Bird RB, Curtis CF, Armstrong RC, Hassager O. Dynamics of Polymeric Liquids, Vol. 1: Fluid Mechanics. 2nd Edition. New York: Wiley; 1987.
18. Malkin AY, Petrie CJS. Some conditions for rupture liquids in extension. *J Rheol*. 1977;41:1–25.
19. Bicerano J. Prediction of Polymer Properties. 3rd Edition. New York:Marcel Dekker; 2002.
20. Kase S, Matsuo T. Studies on melt spinning. II. Steady-state and transient solutions of fundamental equations compared with experimental results. *J Appl Polym Sci*. 1967;11:251–287.

Manuscript received Jun. 3, 2006, and revision received Nov. 1, 2006.